

Article

High Yield Synthesis of Hydroxyapatite (HAP) and Palladium Doped HAP via a Wet Chemical Synthetic Route

Joanna Kamieniak¹, Elena Bernalte^{1,2}, Christopher W. Foster¹, Aidan M. Doyle¹, Peter J. Kelly¹ and Craig E. Banks^{1,*}

¹ Faculty of Science and Engineering, Manchester Metropolitan University, Chester Street, Manchester M1 5GD, UK; joannakamieniak89@gmail.com (J.K.); ebernaltemorgado@gmail.com (E.B.); cwfoster90@gmail.com (C.W.F.); a.m.doyle@mmu.ac.uk (A.M.D.); peter.kelly@mmu.ac.uk (P.J.K.)

² Departamento de Química Analítica e IACYS, Facultad de Ciencias, Universidad de Extremadura, Avda. de Elvas s/n, Badajoz 06006, Spain

* Correspondence: c.banks@mmu.ac.uk; Tel.: +44-161-247-1196; Fax: +44-161-247-6831

Academic Editor: Keith Hohn

Received: 2 July 2016; Accepted: 28 July 2016; Published: 4 August 2016

Abstract: A novel procedure for the synthesis of both hydroxyapatite (HAP) and palladium doped HAP via a wet chemical precipitation method is described herein. X-ray Diffraction (XRD), Raman Spectroscopy, Scanning Electron Microscopy (SEM) with Energy Dispersive X-ray Spectroscopy (EDS) and Fourier Transform Infrared (FT-IR) Spectroscopy are utilised to characterise the synthesised material's morphology, structure and crystallinity. The developed synthetic protocol produces high purity HAP with an average yield of 83.7 (± 0.10)% and an average particle size of 58.2 (± 0.98) nm, such synthesis has been achieved at room temperature and within a time period of less than 24 h. Additionally, in order to enhance the overall conductivity of the material, a range of Pd (2, 4 and 6 wt %) metal doped HAP has been synthesised, characterised and, for the first time, applied towards the competitive electrocatalytic detection of hydrazine, exhibiting a linear range of 50–400 μ M with a limit of detection (3σ) of 30 μ M.

Keywords: hydroxyapatite; palladium; synthesis; hydrazine; electrochemical application

1. Introduction

Hydroxyapatite (HAP), $\text{Ca}_{10}(\text{PO}_4)_6(\text{OH})_2$, is an inorganic compound that has a similar mineral composition to that of human bones and teeth [1]. HAP has been reported to exhibit excellent biocompatibility, bone-bonding ability and also possesses no toxicity or inflammatory response towards the human body [2]. Due to these beneficial attributes, it has widely been investigated within biomedical applications such as a bone/teeth implants, bone tissue regeneration, cell proliferation and drug delivery [3,4]. In addition to these applications, the specific characteristics of HAP, such as low water solubility and high stability under oxidising and reducing conditions, make this material suitable as a sorbent in the purification of wastewater and removal of a variety of heavy metals, such as arsenic (III), selenium (IV), lead (II), cadmium (II), cobalt (II) or nickel (II) from contaminated industrial aqueous waste [5–9]. Another powerful application of HAP is the determination of ammonia for applications such as environmental pollution control, reported by Zhang et al. [10], who describe electrochemical detection of ammonia (at room temperature) using a composite of HAP/graphene which exhibits a significant improvement in the analytical sensitivity compared to that of a bare graphene sensor. Furthermore, Kanchana et al. [11] employed HAP towards the electrochemical detection of uric acid demonstrating a limit of detection of 142 nM, which was applied to human urine and blood serum. These specific applications of HAP require careful control of properties such as

particle size, dimensional anisotropy, morphology, real microstructure etc., all of which are critically important for the optimisation and utilisation of HAP into different fields [12,13].

HAP is a non-conductive inorganic compound and is typically used as a catalyst support for a limited amount of metals/metal oxides [14–16]. In the study reported by Mori et al. [14] palladium nanoclusters were applied onto HAP surfaces and employed towards selective oxidation of alcohols with use of molecular oxygen. Subsequently, palladium metal coupled with HAP was also utilised in Suzuki-Miyaura cross-coupling reactions with sixteen different aryl boronic acids and several different aryl halides, described by Indra et al. [15]. However, it is not only palladium metal that has been successfully assembled with HAP; rhodium supported HAP has also been investigated towards hydrogen generation from the methanolysis of ammonia borane, revealing very high activity [16].

A variety of methods have been developed to synthesise HAP, with the majority employing either wet chemical [17–19], sol-gel [1], hydrolysis [20], microwave irradiation [21] or hydrothermal methods [3,22,23]. However, most of the stated techniques require complicated setups such as reflux or autoclave systems that involve high temperature and pressures; thus the most utilised and proposed method in this report methodology is wet chemical precipitation, due to its low cost, simplicity and reduced energy consumption. Additionally, depending upon the solvents used to maintain the pH during the synthesis different purity yields can be obtained; for example Kavitha et al. [24] utilised tris-(hydroxymethyl)aminomethane to control a constant pH during the synthesis achieving an unsatisfactory yield between 27%–36%. Nevertheless, by maintaining a stable solution pH the crystallinity can be differentiated between flower-like, bowknot-like and monorods, as described by Liu et al. [21], where microwave radiation was used to synthesise HAP; the specific properties for each shape of crystals are still under investigation. It is important to note that the majority of studies do not report specific yields of HAP produced, as summarised within Table 1.

In this paper, a novel wet chemical synthesis protocol for HAP is presented, which is achieved through the combination and optimisation of existing methods, producing HAP with an average yield of 83.7 (± 0.10)% ($N = 3$). This new methodology uses less toxic substrates when compared to previous approaches and is completed within less than 24 h, which is considerably less time compared to other studies (as shown in Table 1). The synthesised HAP has been fully characterised using XRD, Raman Spectroscopy, SEM, EDS, TEM and FT-IR. The synthesis protocol is extended to produce Pd⁰ (2, 4 and 6 wt %) doped HAP that has been synthesised, characterised and for the first time applied towards the electrocatalytic detection of hydrazine.

Table 1. Different approaches for the wet chemical synthesis of hydroxyapatite (HAP) reported within the literature, including solvents employed and yields (where applicable).

Solvent Used to Maintain pH during the Synthesis	Yield %	Comments	Time	Temperature of Synthesis/°C	References
Tris hydroxyl methyl amino methane	27–36	-	Not stated	300–500	[24]
Ammonia	Not stated	Yield stated as high, however no specific value mentioned	~30 h	37	[25]
Ammonia	>75	Starch used to prevent agglomeration of nanoparticles	~40 h	85	[26]
Potassium hydroxide	Not stated	Yield stated as high, however no specific value mentioned	~30 h	70	[27]
Ammonia	Not stated	Yield not stated	~8 days	25–100	[28]
Orthophosphoric acid	Not stated	Yield not stated	~30 h	18–22	[29]
Ammonia and deionised water	Not stated	Yield not stated	>70 h	18–22	[13]
Ammonia	Not stated	Yield not stated	~50 h	95	[30]
Ammonia	Not stated	Yield not stated	~40 h	18–22	[31]
Phosphoric acid	Not stated	Yield not stated	~80 h	18–22	[32]
Sodium hydroxide	84	-	<24 h	18–22	This work

2. Results and Discussion

2.1. Hydroxyapatite (HAP) Synthesis

Hydroxyapatite (HAP) was synthesised as described in the Experimental Procedures section, which is a combination of previously reported studies (shown in Table 1) and optimisation of synthesis time and the solvents used to make the proposed protocol simpler and more efficient with less environmental damage. The obtained material was characterised via SEM, which as depicted within Figure 1A,B reveals a highly agglomerated crystalline HAP structure that is typical of nanocrystal behaviour. The same morphological observations of the HAP has been reported in independent work by Yamini et al. [33] where XRD studies also confirm it belonged to a hexagonal crystal system. As observed on TEM images (shown in Figure 2A) HAP reveals small degree of porosity, but more importantly stable crystalline structure. Following SEM and TEM characterisation, EDS analysis was performed to examine the elemental composition of the materials. Based upon the results as shown within ESI Figure 1, it is clear that the composition of the obtained powder contains the elements Ca, P, O, as expected for HAP, and they are present in the same ratio as that of the stoichiometric reaction. It is important to note that the presence of sodium particles are contributed by the sodium hydroxide solution used to maintain a stable pH over the course of reaction (see Experimental Section).

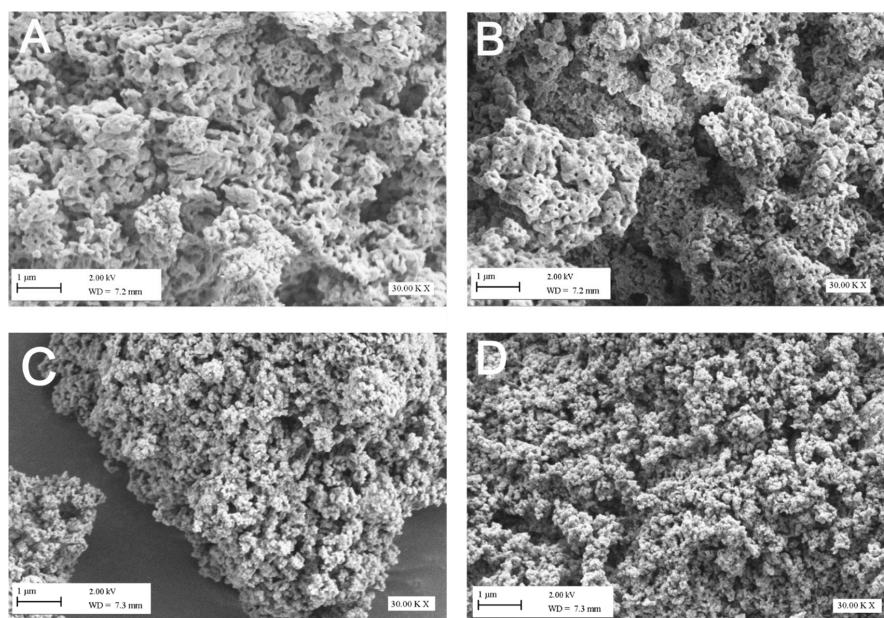


Figure 1. Typical SEM images of HAP (hydroxyapatite) (A,B) and Pd (4 wt %) doped HAP (C,D).

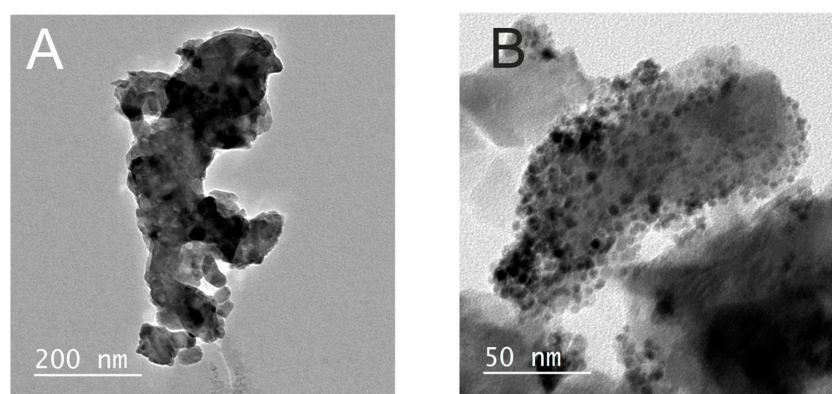


Figure 2. TEM images of HAP (A) and Pd doped HAP (B).

A Raman spectroscopy study was next employed to characterise the synthesised material. As shown in Figure 3A, the spectra is dominated by one sharp peak at 963 cm^{-1} , which represents symmetric stretching mode (ν_3) of the phosphate ions [34]. The 1049 cm^{-1} peak corresponds to the asymmetric stretching mode (ν_3) of the phosphate ions, while the peak at 450 cm^{-1} is due to the symmetric bending mode (ν_2) of the phosphate ions. The final peak at 581 cm^{-1} indicates asymmetric bending mode (ν_4) of the phosphate groups [34]. Subsequently, the crystallinity of HAP was investigated using XRD. The XRD pattern shown within Figure 4A suggests a single crystal structure of hexagonal HAP. This pattern reveals the successful formation of HAP and conforms to the HAP standard (Joint Committee on Powder Diffraction Standards) JCPDS pattern 01-072-1243) shown in Figure 4B and described elsewhere [35]. Such crystals were analysed by a Zetasizer using dynamic light scattering and zeta potential giving an average particle size of $58.2 (\pm 0.98)\text{ nm}$.

Attention was next turned to the spectral characterisation of the HAP via FT-IR, using attenuated total reflectance (ATR) to indicate chemical bonding of the HAP powder and determine any impurities (such as nitrate ions) that are formed during the reaction that could cause contamination of the end product. The double peak present at 599 cm^{-1} and 603 cm^{-1} , as shown in ESI Figure 2, is associated with bending modes in the P–O bonds in the phosphate groups. The peak observed at 1024 cm^{-1} indicates a stretching mode in the P–O bonds within the HAP, which agrees with the reports described elsewhere [36,37]. Therefore, formation of the phosphate group within the synthesised HAP is confirmed via FTIR studies. At the same time, infrared excludes contamination by nitric acid, which were by-products removed by multiple washing steps (using ethanol and deionised water) of the synthesised HAP. This is due to the absence of nitro group peaks, which appear in the range of $1550\text{--}1475\text{ cm}^{-1}$ (asymmetric stretch) and $1360\text{--}1290\text{ cm}^{-1}$ (symmetric stretch) [38].

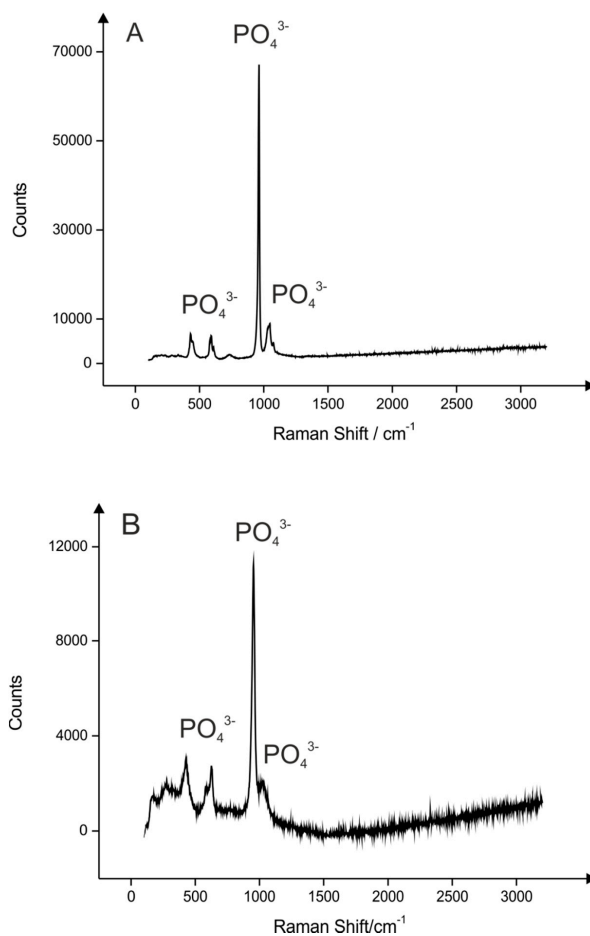


Figure 3. Typical Raman Spectra of the synthesised HAP (A) and Pd (4 wt %) doped HAP (B).

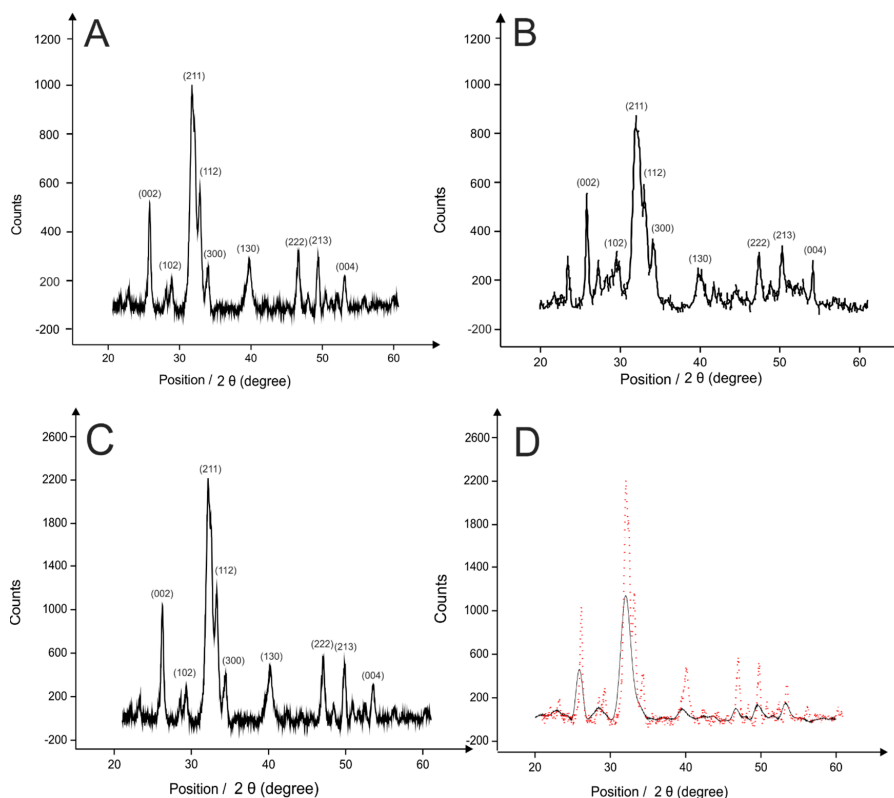


Figure 4. X-ray Diffraction pattern of HAP (A); Standard HAP pattern—JCPDS (Joint Committee on Powder Diffraction Standards) 01-072-1243 (B); Pd (2 wt %) doped HAP (C); HAP (solid line) and Pd doped HAP (dash line) (D) [35].

This wet synthesis approach after optimisation was repeated three times with the average percentage yield found to correspond to 83.7% ($\pm 0.10\%$; $N = 3$), which is extremely high when compared to other literature studies as presented in Table 1. It should be noted that most of the reported studies do not mention a specific value of the yield obtained [28–30,39,40]. Öner et al. [27] reported an approach where they have used less harmful components than ammonia i.e. potassium hydroxide, nevertheless no yield or reproducibility of the proposed method was specified. In comparison to the previously reported strategies, presented within Table 1, this new proposed synthesis is more attractive as it gives rise to a shorter reaction time (<24 h), low temperature synthesis (room temperature) and therefore reduced energy consumption, homogenous mixing, nanophase particle size/shape control and higher product yield. Obtaining high yield in the synthesis is essential to validate the proposed route and demonstrate how reliable and successful the methodology is when compared to theoretical equation of the reaction.

2.2. Palladium Doped HAP

The above approach was to extend the synthesis of HAP with an active metal, in this case palladium, to enhance overall conductivity of the material and at the same time make it capable to perform electrocatalysis. The Pd⁰ doped HAP was synthesised as described in the Experimental Procedures via an ion exchange mechanism using three different amounts of Pd salt to obtain 2, 4 and 6 wt % modified HAP. The SEM images revealed the morphology of the particulates remained the same after application of the palladium metal upon the HAP surface (Figure 1C,D). As shown on TEM images (Figure 2B) palladium has been uniformly distributed throughout the sample demonstrating the reliability of ion exchange loading method. Raman Spectroscopy of the palladium doped HAP confirm that the phosphate groups within HAP structure persist unchanged as shown in Figure 3B,

however the intensity of the peaks decreased significantly due to changes in the centre of symmetry of the material. As described before HAP possesses hexagonal crystal structure, however introducing metal into the system results in asymmetry in the system, therefore crystallinity of the material is decreased giving reduced intensity peaks [41]. XRD analysis showed larger crystal formation due to the palladium metal deposited upon the HAP surface, indicated by sharper (narrower) XRD peaks, when compared to the JCPDS pattern presented in Figure 4B,C. Also, patterns reveal face-centred-cubic crystalline palladium metal, with all the peaks shifted slightly, corresponding to a lower binding energy of the material (shown in Figure 4D) [42,43]. This scenario is also accompanied by an increased intensity of the peaks, which is characteristic behaviour for material with changed centre of symmetry of the material. Next, based on the XRD patterns from the varied amounts of Pd⁰ loaded on the HAP, the peak that corresponds to the metal, at 40 degrees 2θ, clearly increases with additions of palladium on the surface of HAP during the synthesis (Figure 5A,B), indicating higher concentrations of palladium metal in the end product.

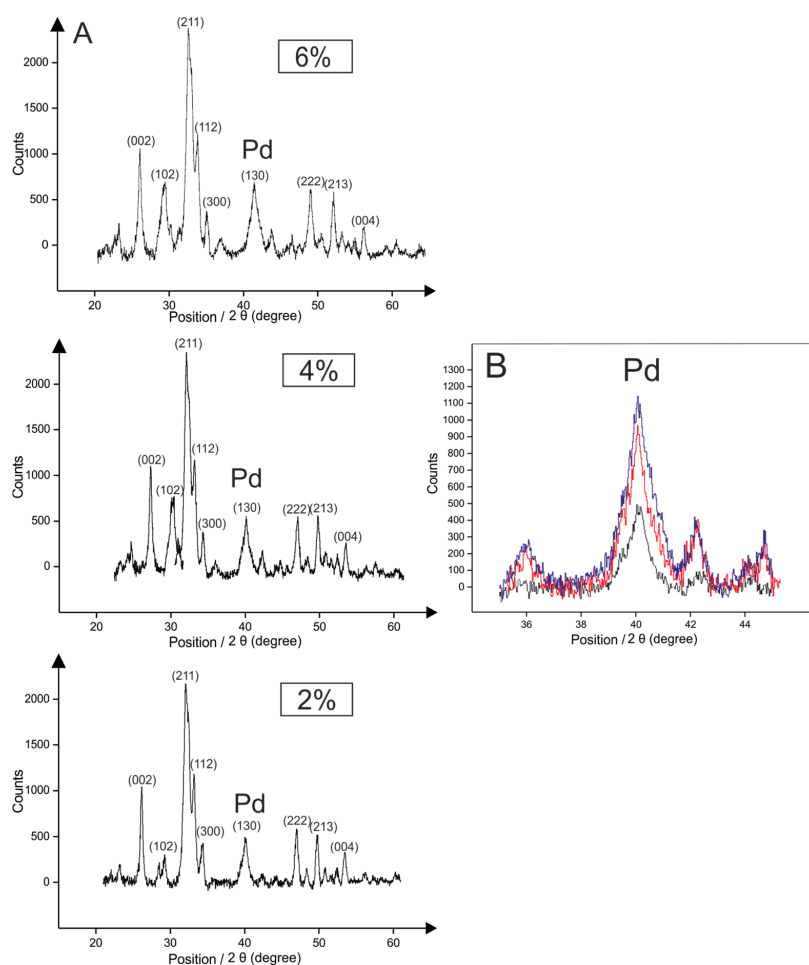


Figure 5. X-ray diffraction pattern of different Pd loadings (2, 4, 6 wt %) upon HAP (A) with 2 wt % (black line); 4 wt % (red line) and 6 wt % (blue line) of metal in the on the surface of HAP (B).

2.3. Application of Pd⁰ Doped HAP

Following the described synthesis of the Pd doped HAP, attention was next turned to the application of the material towards the electrochemical detection of hydrazine. Hydrazine is described as a very powerful reducing agent that is widely used in many different industries [44]. According to the Environmental Protection Agency (EPA), it is recognised as an environmental pollutant due to its toxicity and its tendency to act as an irritant [45]. Humans can be exposed to hydrazine via drinking

contaminated water, inhaling contaminated air, or even from swallowing and touching contaminated dust [46]. Severe exposure to hydrazine is detrimental to the liver, kidneys and central nervous system; therefore, there is a need for a reliable, fast and simple electrochemical sensing platform for the detection of hydrazine [45].

Figure 6A represents a linear sweep voltammogram recorded in a pH 7.4 PBS containing 0.5 M hydrazine using Pd (4 wt %) doped HAP modified screen-printed electrode (Pd/HAP/SPE) in comparison to the bare SPE in the same aqueous solution. As described previously upon palladium metal surfaces the electrochemical oxidation of hydrazine involves transfer of 4 electrons per molecule leading to the production of nitrogen [47]. It can be observed in Figure 6A, that the bare SPE was first examined in order to evaluate its suitability to detect hydrazine, with an analytical signal, unlike when the electrode was modified with Pd doped HAP where significant increase in current is observed demonstrating the catalytic role towards the material. In the study by Batchelor-McAuley et al. [48], the application of pure Pd nanoparticle modified electrode the electrochemical oxidation of hydrazine was reported to occur at a peak potential at $\sim +0.2$ V (vs. SCE). In this study the electrochemical oxidation of hydrazine was found to occur $\sim +0.5$ V (vs. SCE) which indicates an overpotential is required to drive the electrochemical reaction which is likely due to a sparsely distributed Pd over the HAP. Note that this approach has taken an inert material (i.e., HAP) and transformed it into a useful electrochemical material. This is reflected in the difference in the overpotential observed in our work, which is higher than prior literature. Unlike previously reported studies, where the employed materials have always been conductive i.e., graphene/carbon nanotubes on standard glassy carbon electrode, as listed in Table 2, this work for the first time combines a new material described above on a disposable, easy to use and low cost screen-printed electrochemical platform.

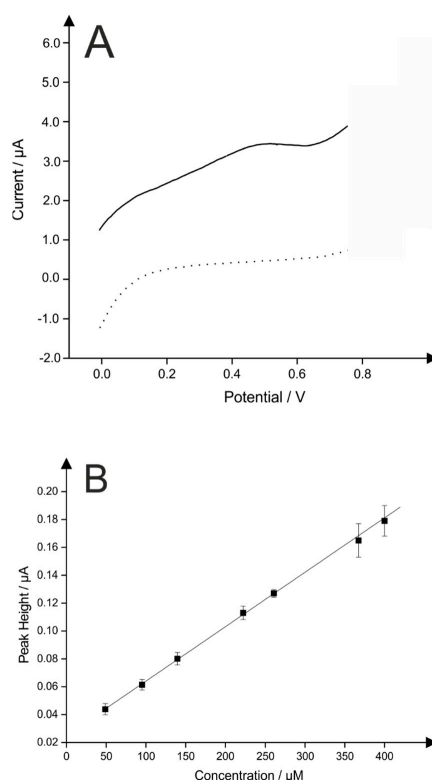


Figure 6. Typical linear sweep voltammogram (LSV) representing bare SPE (graphitic screen-printed electrode) in buffer solution (dashed line) and Pd (4 wt %) doped HAP modified SPE (50 μg) (solid line) in a pH 7.4 PBS (phosphate buffered solution) in the presence of 500 μM hydrazine (A); Calibration plot (B). Error bars indicate a standard deviation of $N = 3$. Scan rate: $5 \text{ mV} \cdot \text{s}^{-1}$ vs. SCE. Note that each data point on calibration plot (B) represents new electrode utilised.

Table 2. Plethora of palladium metal modified surfaces employed for hydrazine detection with limits of detection and electrochemical methods used. The following abbreviations are used: glassy carbon electrode (GCE), cyclic voltammetry (CV), linear sweep voltammetry (LSV), ethylenediamine cellulose (EDAC), polyaniline (PANI), boron-doped diamond (BDD), basal plane pyrolytic graphite electrode (BPPG).

Metal	Pd Loading/wt %	Support	Electrode	Electrochemical Method	Linear Range/ μM	LOD (3σ)/ μM	References
Au/Pd	Not stated	TiO ₂ nanotubes	GCE	CV	0.06–700	12	[49]
Pd	20.6	Carbon nanotubes	GCE	CV	2.5–700	1	[50]
Pd	100	PANI	GCE	CV	10–300	0.5	[51]
Pd	0.6	Carbon black	GCE	CV	5–50	8.8	[47]
Pd	100	Not stated	MWCNT	LSV	56–157	10	[52]
Pd	100	Not stated	BDD	LSV	27.2–85	2.6	[53]
Pd/Au/Ag	Not stated	Glassy Carbon Microspheres	BPPG	CV	0–300	4	[54]
Pd	Not stated	Graphene	GCE	CV	1–740	17	[55]
Pd	Not stated	Guar gum	GCE	CV	50–600	4.1	[56]
Au/Pd	Not stated	Graphene nanoplatelets	GCE	CV	Not stated	Not stated	[57]
Pd	7.3	EDAC	GCE	CV	5–150	1.5	[58]
Pd	4	HAP	SPE	LSV	50–400	30	This work

It was observed that the first material tested (i.e., 2 wt % of Pd) gave random and unreproducible electrochemical signals. It was clear that the amount of metal in the material was insufficient to detect hydrazine accurately even though oxidation signals were recorded. Subsequently, the last material synthesised (i.e. 6 wt % of Pd) revealed good reproducibility over the range of electrodes tested ($N = 3$), however at lower coverages the peak potential possessed a large percentage error and a lower peak current when compared to 4 wt % (shown in ESI Figure 3). Hence, it was demonstrated that the best metal loading on the HAP surface with the best reproducibility of the electrocatalytic determination of hydrazine, using different electrodes and different coverages was 4 wt % of Pd upon the HAP surface. In terms of intensity of the peak current, it was noted that the best coverage on SPE using such material corresponded to 10 μL (50 μg immobilised upon the electrode surface). Therefore, it was selected for further tests.

Next, the voltammetric detection of hydrazine was explored with additions made into pH 7.4 phosphate buffered solution where the voltammetric signal was monitored as a function of concentration. Consequently, a plot of the oxidation peak height vs. hydrazine concentration was constructed and illustrated in Figure 6B, using the optimised 4 wt % Pd upon HAP modified SPE. Note, that regarding the disposable character of screen printed electrodes, they were used as one shot sensors, thus three different electrodes were used for different concentrations of hydrazine giving non-significant variations (shown as standard deviations in Figure 6B). The plot reveals a linear response over the concentration range of 50–400 μM hydrazine, ($I_H/\mu\text{A} = 0.3904 \times 10^{-4} \mu\text{A} \cdot \mu\text{M}^{-1} + 0.0025 \mu\text{A}$; $R^2 = 0.9994$; $N = 7$). It was additionally noted, that the lowest detectable concentration of hydrazine in this study was found to be 50 μM with a (limit of detection) LOD (3σ) of 30 μM , which is higher in comparison to a study published by Zhao et al. [50] and Ejaz et al. [55] with a LOD of 12 μM and 17 μM , respectively. However, it worth to note that both studies utilised traditional electrochemical setup i.e., glassy carbon electrode and employed conductive supports such carbon nanotubes or graphene. The modification of low cost, easy to use and portable screen-printed electrodes with Pd (4 wt %) doped HAP was demonstrated to be electrochemically useful, when HAP has been transformed from inert material into a semi-conductive material that has been successfully applied for the electroanalytical detection of hydrazine, demonstrating to be a suitable and low production cost analytical sensor. It is clear that the more expensive pure palladium alternatives offer further beneficial electrochemical responses with lower LOD, these reports are summarised in Table 2. However, in terms of production costs, this reported novel synthesis and material still proves beneficial and competitive for the application of a low Pd hydrazine sensor; the low metallic Pd content (4 wt %) makes this material an remarkably attractive alternative to existing Pd modified electrodes.

3. Experimental Procedures

3.1. Materials and Chemicals

All chemicals were obtained from Sigma-Aldrich (Dorset, UK) and were used as received without any further purification. All solutions were made by using deionised water with resistivity not less than 18.2 $\text{M}\Omega\text{-cm}$.

3.2. Synthesis of HAP

$(\text{NH}_4)_2\text{HPO}_4$ (0.4 M, 100 mL) was stirred at room temperature (18–22 $^\circ\text{C}$) in a 2 L beaker with $\text{Ca}(\text{NO}_3)_2$ (0.6 M, 100 mL) added dropwise over one hour, resulting in a “milky” suspension of HAP. The Ca/P molar ratio was kept at 1.67 corresponding to the stoichiometry of HAP. The pH was maintained through the addition of NaOH (0.1 M) within the range 9.4–9.5. This “milky” suspension was then stirred overnight at room temperature using a magnetic stirring bar. The obtained precipitate was filtered, cleaned alternately with water and ethanol three times, oven dried at 65 $^\circ\text{C}$ for six hours, and then calcined at 600 $^\circ\text{C}$ for a further two hours making full synthesis complete within less than 24 h.

3.3. Synthesis of Pd⁰ Doped HAP

First, Pd(NO₃)₂ (50, 100 and 150 mg) was dissolved in 100 mL of deionised water, after which the HAP was added (1 g) and the resulting mixture was stirred for three days at room temperature (ion exchange), filtered and vacuum dried. The obtained PdO upon HAP appeared as a yellow powder, which was then reduced to Pd⁰ through introduction of a flow of hydrogen (30 mL·min⁻¹) at 300 °C using a chemical vapour deposition (CVD) rig with a rotary pump (Carbolite type 3216, Tempatron, PID500/110/330, Essex, UK) to obtain a pressure of 1000 Pa. The excess of hydrogen was removed from the surface using argon atmosphere and the sample was cooled to room temperature under the same conditions. The end product was observed to be a grey powder [59,60].

3.4. Electrochemical Measurements

Experiments were performed using a typical three-electrode system (supplier, city, country), consisting of a graphitic screen-printed electrode (SPE) working surface (3 mm diameter), platinum wire counter electrode and a saturated calomel electrode (SCE) as the reference completing the circuit.

The SPEs were fabricated in-house with appropriate stencil designs using a microDEK 1760RS screen-printing machine (DEK, Weymouth, UK). For each of the screen-printed sensors a carbon-graphite ink formulation was first screen-printed onto a polyester flexible film (Autostat, 250 µm thickness). This layer was cured in a fan oven at 60 °C for 30 min. Next a silver/silver chloride (40:60) pseudo-reference electrode was applied by screen-printing Ag/AgCl paste (Product Code: C2040308P2; Gwent Electronic Materials Ltd., Pontypool, UK) onto the plastic substrate. This layer was once more cured in a fan oven at 60 °C for 30 min. Last a dielectric paste ink (Product Code: D2070423P5; Gwent Electronic Materials Ltd., Pontypool, UK) was printed to cover the connections and define the 3 mm diameter graphite working electrode. After curing at 60 °C for 30 min the screen-printed electrode was ready to use [61].

The SPE was then precisely cut to remove the Ag/AgCl pseudo-reference and carbon counter allowing for modification of Pd doped HAP using the drop-coating method; an external SCE and counter electrode were then utilised for electrochemical studies. Linear Sweep Voltammetry (LSV) method was carried out in the range of 0 to +0.8 V at the scan rate 5 mV·s⁻¹ vs. SCE. The dispersed Pd (2, 4 and 6 wt %) doped HAP was dissolved in a mixture of ethanol-water (50:50) to obtain a final concentration of 0.5 mg·mL⁻¹ and was gently sonicated. Aliquots (2 µL at a time) were then pipetted into the surface of the working electrode and dried in an oven below 40 °C. Each modification was repeated on three different electrodes to examine reproducibility of the different coverages assayed. Hydrazine solution (500 µM) in a pH 7.4 phosphate buffered solution (PBS) was employed as an analyte throughout the electrochemical tests. Voltammetric measurements were carried out using an µ-AUTOLAB III (ECO-Chemie, Utrecht, The Netherlands) potentiostat. All measurements were performed at 25 °C. In addition an edge-connector was used to ensure the reproducibility of the electrochemical connections throughout the studies [61].

3.5. Characterisation of the HAP and Pd⁰ Doped HAP

The structure, crystallography and morphology of the synthesised HAP and Pd doped HAP particles were analysed using various of techniques. Scanning Electron Microscopy (SEM) images were obtained with a Supra 40VP model SEM (Carl Zeiss Ltd., Cambridge, UK) coupled to an Apollo 40 SDD energy-dispersive X-ray microscope (EDAX, Cambridge, UK) to estimate surface elemental composition of HAP and Pd content; Transmission Electron Microscopy (TEM) (JEOL JEM 2100 using 200 kV, Akishima, Tokyo) images were acquired to study the surface morphology of the samples by dispersing the particles in ethanol and sonicating one hour before drying on the TEM grid. After evaporation of the solvent sample was cleaned using plasma etching system; Raman Spectroscopy was performed using a “inVia” confocal Raman Microscope (Reinshaw PLC, York, UK) equipped with a confocal microscope (×50 objective) spectrometer with an argon laser (514 nm excitation)

and a very low laser power level (0.8 mW) to avoid any heating effects to examine stretching and bending modes within the molecule. Fourier transform infrared spectroscopy (FT-IR) (Nicolet 380 Smart iTR, Waltham, USA) used diamond attenuated total reflection (ATR) diamond detector without any further purification of sample to confirm formation of the phosphate groups within HAP; X-ray Diffraction (XRD) (X'Pert Powder, PANalytical, Cambridge, UK) was used in powder spinning mode to distinguish the crystallinity of the material and confirm formation and phase purity of both HAP and Pd. The angle of the anti-scatter slit was 1° and the 2θ range measured was between 20° – 60° using Cu-K α radiation, with a step size of 0.052° and 200 s/step. A Zeta sizer (Nano series, NanoZS, Malvern Instruments, Malvern, UK) was used to estimate the size of the HAP particles.

4. Conclusions

This paper has reported a novel wet chemical synthesis of HAP with a high average yield of 83.7 (± 0.10)% with an average particle size of 58.2 ± 0.98 nm. It is not only the yield that makes this approach extremely attractive, but also low temperature synthesis, low cost, simplicity of the method, homogenous mixing and nanophase particle size control resulting in a very pure phase of HAP. Characterisation of HAP nanocrystals indicated that the synthesised material was pure and crystalline with a Raman spectra revealing successful formation of the phosphate groups within the HAP crystals. This was also demonstrated by XRD, where patterns showed that HAP possessed a single crystalline structure, however by adding palladium upon the surface, crystals become larger causing more intense and sharper peaks. Also, the excellent purity of crystals obtained applying the methodology proposed in this work was confirmed by FT-IR where potential nitro impurities were not present. Finally, the modification of low cost, easy to use and portable screen-printed electrodes with Pd (4 wt %) doped HAP was demonstrated to be electrochemically useful, when HAP has been transformed from inert material into a semi-conductive that has been successfully applied for the electroanalytical detection of hydrazine, demonstrating to be a suitable and low production cost analytical sensor.

Author Contributions: J.K. performed experiments and wrote the manuscript. The electrochemical data was analysed by E.B. and contributed to the writing of the paper. The screen-printed electrodes were prepared by C.W.F. Textural support was provided by C.E.B., A.M.D. and P.J.K. C.E.B conceived and designed the experiments. All authors have given approval to the final version of the manuscript.

Conflicts of Interest: The authors declare no conflict of interest.

References

1. Feng, Y.; Yin, H.; Gao, D.; Wang, A.; Shen, L.; Meng, M. Selective oxidation of 1,2-propanediol to lactic acid catalyzed by hydroxylapatite nanorod-supported au/pd bimetallic nanoparticles under atmospheric pressure. *J. Catal.* **2014**, *316*, 67–77. [[CrossRef](#)]
2. Bellucci, D.; Sola, A.; Gazzarri, M.; Chiellini, F.; Cannillo, V. A new hydroxyapatite-based biocomposite for bone replacement. *Mater. Sci. Eng. C* **2013**, *33*, 1091–1101. [[CrossRef](#)] [[PubMed](#)]
3. Wu, S.-C.; Tsou, H.-K.; Hsu, H.-C.; Hsu, S.-K.; Liou, S.-P.; Ho, W.-F. A hydrothermal synthesis of eggshell and fruit waste extract to produce nanosized hydroxyapatite. *Ceram. Int.* **2013**, *39*, 8183–8188. [[CrossRef](#)]
4. Loca, D.; Locs, J.; Dubnika, A.; Zalite, V.; Berzina-Cimdina, L. 9-porous hydroxyapatite for drug delivery. In *Hydroxyapatite (hap) for biomedical applications*; Mucalo, M., Ed.; Woodhead Publishing: Cambridge, UK, 2015; pp. 189–209.
5. Kongsri, S.; Janpradit, K.; Buapa, K.; Techawongstien, S.; Chanthai, S. Nanocrystalline hydroxyapatite from fish scale waste: Preparation, characterization and application for selenium adsorption in aqueous solution. *Chem. Eng. J.* **2013**, *215–216*, 522–532. [[CrossRef](#)]
6. Vila, M.; Sánchez-Salcedo, S.; Vallet-Regí, M. Hydroxyapatite foams for the immobilization of heavy metals: From waters to the human body. *Inorg. Chim. Acta* **2012**, *393*, 24–35. [[CrossRef](#)]

7. Gupta, N.; Kushwaha, A.K.; Chattopadhyaya, M.C. Adsorptive removal of Pb^{2+} , Co^{2+} and Ni^{2+} by hydroxyapatite/chitosan composite from aqueous solution. *J. Taiwan Inst. Chem. Eng.* **2012**, *43*, 125–131. [[CrossRef](#)]
8. Salah, T.A.; Mohammad, A.M.; Hassan, M.A.; El-Anadouli, B.E. Development of nano-hydroxyapatite/chitosan composite for cadmium ions removal in wastewater treatment. *J. Taiwan Inst. Chem. Eng.* **2014**, *45*, 1571–1577. [[CrossRef](#)]
9. Zhang, Y.; Liu, Y.; Ji, X.; Banks, C.E.; Zhang, W. Conversion of natural egg-shell to 3d flower-like hydroxyapatite agglomerates for highly sensitive detection of As^{3+} ions. *Mater. Lett.* **2012**, *78*, 120–123. [[CrossRef](#)]
10. Zhang, Q.; Liu, Y.; Zhang, Y.; Li, H.; Tan, Y.; Luo, L.; Duan, J.; Li, K.; Banks, C.E. Facile and controllable synthesis of hydroxyapatite/graphene hybrid materials with enhanced sensing performance towards ammonia. *Analyst* **2015**, *140*, 5235–5242. [[CrossRef](#)] [[PubMed](#)]
11. Kanchana, P.; Sekar, C. Edta assisted synthesis of hydroxyapatite nanoparticles for electrochemical sensing of uric acid. *Mater. Sci. Eng. C* **2014**, *42*, 601–607. [[CrossRef](#)] [[PubMed](#)]
12. Ghosh, S.K.; Roy, S.K.; Kundu, B.; Datta, S.; Basu, D. Synthesis of nano-sized hydroxyapatite powders through solution combustion route under different reaction conditions. *Mater. Sci. Eng. B* **2011**, *176*, 14–21. [[CrossRef](#)]
13. Padmanabhan, S.K.; Balakrishnan, A.; Chu, M.C.; Lee, Y.J.; Kim, T.N.; Cho, S.J. Sol-gel synthesis and characterization of hydroxyapatite nanorods. *Particuology* **2009**, *7*, 466–470. [[CrossRef](#)]
14. Mori, K.; Hara, T.; Mizugaki, T.; Ebitani, K.; Kaneda, K. Hydroxyapatite-supported palladium nanoclusters: A highly active heterogeneous catalyst for selective oxidation of alcohols by use of molecular oxygen. *J. Am. Chem. Soc.* **2004**, *126*, 10657–10666. [[CrossRef](#)] [[PubMed](#)]
15. Indra, A.; Gopinath, C.S.; Bhaduri, S.; Kumar Lahiri, G. Hydroxyapatite supported palladium catalysts for suzuki-miyaura cross-coupling reaction in aqueous medium. *Catal. Sci. Technol.* **2013**, *3*, 1625–1633. [[CrossRef](#)]
16. Özhava, D.; Özkar, S. Rhodium(0) nanoparticles supported on hydroxyapatite nanospheres and further stabilized by dihydrogen phosphate ion: A highly active catalyst in hydrogen generation from the methanolysis of ammonia borane. *Int. J. Hydrogen Energy* **2015**, *40*, 10491–10501. [[CrossRef](#)]
17. Andrasekhar, A.; Sagadevan, S.; Dakshnamoorthy, A. Synthesis and characterisation of nano-hydroxyapatite (n-hap) using the wet chemical technique. *Int. J. Phys. Sci.* **2013**, *8*, 1639–1645.
18. Kamalanathan, P.; Ramesh, S.; Bang, L.T.; Niakan, A.; Tan, C.Y.; Purbolaksono, J.; Chandran, H.; Teng, W.D. Synthesis and sintering of hydroxyapatite derived from eggshells as a calcium precursor. *Ceram. Int.* **2014**, *40*, 16349–16359. [[CrossRef](#)]
19. Wang, P.; Li, C.; Gong, H.; Jiang, X.; Wang, H.; Li, K. Effects of synthesis conditions on the morphology of hydroxyapatite nanoparticles produced by wet chemical process. *Powder Technol.* **2010**, *203*, 315–321. [[CrossRef](#)]
20. Bahrololoom, M.E.; Javidi, M.; Javadpour, S.; Ma, J. Characterisation of natural hydroxyapatite extracted from bovine cortical bone ash. *J. Ceram. Process. Res.* **2009**, *10*, 129–138.
21. Liu, J.; Li, K.; Wang, H.; Zhu, M.; Yan, H. Rapid formation of hydroxyapatite nanostructures by microwave irradiation. *Chem. Phys. Lett.* **2004**, *396*, 429–432. [[CrossRef](#)]
22. Wang, Y.; Ren, X.; Ma, X.; Su, W.; Zhang, Y.; Sun, X.; Li, X. Alginate-intervened hydrothermal synthesis of hydroxyapatite nanocrystals with nanopores. *Cryst. Growth Des.* **2015**, *15*, 1949–1956. [[CrossRef](#)]
23. Ji, X.; Su, P.; Liu, C.; Song, J.; Liu, C.; Li, J.; Tan, H.; Wu, F.; Yang, L.; Fu, R.; et al. A novel ethanol induced and stabilized hierarchical nanorods: Hydroxyapatite nanopeanut. *J. Am. Ceram. Soc.* **2015**, *98*, 1702–1705. [[CrossRef](#)]
24. Kavitha, M.; Subramanian, R.; Narayanan, R.; Udhayabanu, V. Solution combustion synthesis and characterization of strontium substituted hydroxyapatite nanocrystals. *Powder Technol.* **2014**, *253*, 129–137. [[CrossRef](#)]
25. Dhand, V.; Rhee, K.Y.; Park, S.J. The facile and low temperature synthesis of nanophase hydroxyapatite crystals using wet chemistry. *Mater. Sci. Eng. C* **2014**, *36*, 152–159. [[CrossRef](#)] [[PubMed](#)]
26. Yang, L.; Ning, X.; Bai, Y.; Jia, W. A scalable synthesis of non-agglomerated and low-aspect ratio hydroxyapatite nanocrystals using gelatinized starch matrix. *Mater. Lett.* **2013**, *113*, 142–145. [[CrossRef](#)]
27. Öner, M.; Uysal, U. Synthesis of hydroxyapatite crystals using carboxymethyl inulin for use as a delivery of ibuprofen. *Mater. Sci. Eng. C* **2013**, *33*, 482–489. [[CrossRef](#)] [[PubMed](#)]

28. Kothapalli, C.; Wei, M.; Vasiliev, A.; Shaw, M.T. Influence of temperature and concentration on the sintering behavior and mechanical properties of hydroxyapatite. *Acta Mater.* **2004**, *52*, 5655–5663. [[CrossRef](#)]
29. Ramesh, S.; Tan, C.Y.; Tolouei, R.; Amiriyani, M.; Purbolaksono, J.; Sopyan, I.; Teng, W.D. Sintering behavior of hydroxyapatite prepared from different routes. *Mater. Des.* **2012**, *34*, 148–154. [[CrossRef](#)]
30. Landi, E.; Celotti, G.; Logroscino, G.; Tampieri, A. Carbonated hydroxyapatite as bone substitute. *J. Eur. Ceram. Soc.* **2003**, *23*, 2931–2937. [[CrossRef](#)]
31. Okada, M.; Furuzono, T. Low-temperature synthesis of nanoparticle-assembled, transparent, and low-crystallized hydroxyapatite blocks. *J. Colloid Interface Sci.* **2011**, *360*, 457–462. [[CrossRef](#)] [[PubMed](#)]
32. Abert, J.; Bergmann, C.; Fischer, H. Wet chemical synthesis of strontium-substituted hydroxyapatite and its influence on the mechanical and biological properties. *Ceram. Int.* **2014**, *40*, 9195–9203. [[CrossRef](#)]
33. Yamini, D.; Devanand Venkatasubbu, G.; Kumar, J.; Ramakrishnan, V. Raman scattering studies on peg functionalized hydroxyapatite nanoparticles. *Spectrochim. Acta Part A Mol. Biomol. Spectrosc.* **2014**, *117*, 299–303. [[CrossRef](#)] [[PubMed](#)]
34. Craig, A.P.; Franca, A.S.; Irudayaraj, J. 7-vibrational spectroscopy for food quality and safety screening. In *High throughput Screening for Food Safety Assessment*; Bhunia, A.K., Kim, M.S., Taitt, C.R., Eds.; Woodhead Publishing: Cambridge, UK, 2015; pp. 165–194.
35. Mohandes, F.; Salavati-Niasari, M.; Fathi, M.; Fereshteh, Z. Hydroxyapatite nanocrystals: Simple preparation, characterization and formation mechanism. *Mater. Sci. Eng. C* **2014**, *45*, 29–36. [[CrossRef](#)] [[PubMed](#)]
36. Ramanan, S.R.; Venkatesh, R. A study of hydroxyapatite fibers prepared via sol–gel route. *Mater. Lett.* **2004**, *58*, 3320–3323. [[CrossRef](#)]
37. Sargin, Y.; Kizilyalli, M.; Telli, C.; Güler, H. A new method for the solid-state synthesis of tetracalcium phosphate, a dental cement: X-ray powder diffraction and ir studies. *J. Eur. Ceram. Soc.* **1997**, *17*, 963–970. [[CrossRef](#)]
38. Javadi, A.; Shokravi, A.; Koohgard, M.; Malek, A.; Shourkaei, F.A.; Ando, S. Nitro-substituted polyamides: A new class of transparent and highly refractive materials. *Eur. Polym. J.* **2015**, *66*, 328–341. [[CrossRef](#)]
39. Arul, K.T.; Ramya, J.R.; Bhalerao, G.M.; Kalkura, S.N. Physicochemical characterization of the superhydrophilic, magnesium and silver ions co-incorporated nanocrystalline hydroxyapatite, synthesized by microwave processing. *Ceram. Int.* **2014**, *40*, 13771–13779. [[CrossRef](#)]
40. Nazir, R.; Iqbal, N.; Khan, A.S.; Akram, A.; Asif, A.; Chaudhry, A.A.; Rehman, I.U.; Hussain, R. Rapid synthesis of thermally stable hydroxyapatite. *Ceram. Int.* **2012**, *38*, 457–462. [[CrossRef](#)]
41. Gutowska, I.; Machoy, Z.; Machalinski, B. The role of bivalent metals in hydroxyapatite structures as revealed by molecular modeling with the hyperchem software. *J. Biomed. Mater. Res. A* **2005**, *75*, 788–793. [[CrossRef](#)] [[PubMed](#)]
42. Li, Y.A.; Tai, N.H.; Chen, S.K.; Tsai, T.Y. Enhancing the electrical conductivity of carbon-nanotube-based transparent conductive films using functionalized few-walled carbon nanotubes decorated with palladium nanoparticles as fillers. *ACS Nano* **2011**, *5*, 6500–6506. [[CrossRef](#)] [[PubMed](#)]
43. Cui, Q.; Chao, S.; Bai, Z.; Yan, H.; Wang, K.; Yang, L. Based on a new support for synthesis of highly efficient palladium/hydroxyapatite catalyst for ethanol electrooxidation. *Electrochim. Acta* **2014**, *132*, 31–36. [[CrossRef](#)]
44. Tang, Y.Y.; Kao, C.L.; Chen, P.Y. Electrochemical detection of hydrazine using a highly sensitive nanoporous gold electrode. *Anal. Chim. Acta* **2012**, *711*, 32–39. [[CrossRef](#)] [[PubMed](#)]
45. Zelnick, S.D.; Mattie, D.R.; Stepaniak, P.C. Occupational exposure to hydrazines: Treatment of acute central nervous system toxicity. *Aviat. Space Environ. Med.* **2003**, *74*, 1285–1291. [[PubMed](#)]
46. Choudhary, G.; Hansen, H. Human health perspective of environmental exposure to hydrazines: A review. *Chemosphere* **1998**, *37*, 801–843. [[CrossRef](#)]
47. Panchompoo, J.; Aldous, L.; Downing, C.; Crossley, A.; Compton, R.G. Facile synthesis of pd nanoparticle modified carbon black for electroanalysis: Application to the detection of hydrazine. *Electroanalysis* **2011**, *23*, 1568–1578. [[CrossRef](#)]
48. Rakap, M.; Özkaz, S. Hydroxyapatite-supported cobalt(0) nanoclusters as efficient and cost-effective catalyst for hydrogen generation from the hydrolysis of both sodium borohydride and ammonia-borane. *Catal. Today* **2012**, *183*, 17–25. [[CrossRef](#)]

49. Chen, X.; Liu, W.; Tang, L.; Wang, J.; Pan, H.; Du, M. Electrochemical sensor for detection of hydrazine based on au@pd core-shell nanoparticles supported on amino-functionalized tio2 nanotubes. *Mater. Sci. Eng. C* **2014**, *34*, 304–310. [[CrossRef](#)] [[PubMed](#)]
50. Zhao, J.; Zhu, M.; Zheng, M.; Tang, Y.; Chen, Y.; Lu, T. Electrocatalytic oxidation and detection of hydrazine at carbon nanotube-supported palladium nanoparticles in strong acidic solution conditions. *Electrochim. Acta* **2011**, *56*, 4930–4936. [[CrossRef](#)]
51. Ivanov, S.; Lange, U.; Tsakova, V.; Mirsky, V.M. Electrocatalytically active nanocomposite from palladium nanoparticles and polyaniline: Oxidation of hydrazine. *Sens. Actuators B Chem.* **2010**, *150*, 271–278. [[CrossRef](#)]
52. Ji, X.; Banks, C.E.; Holloway, A.F.; Jurkschat, K.; Thorogood, C.A.; Wildgoose, G.G.; Compton, R.G. Palladium sub-nanoparticle decorated ‘bamboo’ multi-walled carbon nanotubes exhibit electrochemical metastability: Voltammetric sensing in otherwise inaccessible ph ranges. *Electroanalysis* **2006**, *18*, 2481–2485. [[CrossRef](#)]
53. Batchelor-McAuley, C.; Banks, C.E.; Simm, A.O.; Jones, T.G.J.; Compton, R.G. The electroanalytical detection of hydrazine: A comparison of the use of palladium nanoparticles supported on boron-doped diamond and palladium plated bdd microdisc array. *Analyst* **2006**, *131*, 106–110. [[CrossRef](#)] [[PubMed](#)]
54. Baron, R.; Šljukić, B.; Salter, C.; Crossley, A.; Compton, R.G. Development of an electrochemical sensor nanoarray for hydrazine detection using a combinatorial approach. *Electroanalysis* **2007**, *19*, 1062–1068. [[CrossRef](#)]
55. Ejaz, A.; Ahmed, M.S.; Jeon, S. Highly efficient benzylamine functionalized graphene supported palladium for electrocatalytic hydrazine determination. *Sens. Actuators B Chem.* **2015**, *221*, 1256–1263. [[CrossRef](#)]
56. Rastogi, P.K.; Ganesan, V.; Krishnamoorthi, S. Palladium nanoparticles decorated gaur gum based hybrid material for electrocatalytic hydrazine determination. *Electrochim. Acta* **2014**, *125*, 593–600. [[CrossRef](#)]
57. Wan, Q.; Liu, Y.; Wang, Z.; Wei, W.; Li, B.; Zou, J.; Yang, N. Graphene nanoplatelets supported metal nanoparticles for electrochemical oxidation of hydrazine. *Electrochem. Commun.* **2013**, *29*, 29–32. [[CrossRef](#)]
58. Ahmar, H.; Keshipour, S.; Hosseini, H.; Fakhari, A.R.; Shaabani, A.; Bagheri, A. Electrocatalytic oxidation of hydrazine at glassy carbon electrode modified with ethylenediamine cellulose immobilized palladium nanoparticles. *J. Electroanal. Chem.* **2013**, *690*, 96–103. [[CrossRef](#)]
59. Gauthard, F.; Epron, F.; Barbier, J. Palladium and platinum-based catalysts in the catalytic reduction of nitrate in water: Effect of copper, silver, or gold addition. *J. Catal.* **2003**, *220*, 182–191. [[CrossRef](#)]
60. Rakap, M.; Özkar, S. Hydroxyapatite-supported palladium(0) nanoclusters as effective and reusable catalyst for hydrogen generation from the hydrolysis of ammonia-borane. *Int. J. Hydrogen Energy* **2011**, *36*, 7019–7027. [[CrossRef](#)]
61. Galdino, F.E.; Foster, C.W.; Bonacin, J.A.; Banks, C.E. Exploring the electrical wiring of screen-printed configurations utilised in electroanalysis. *Anal. Methods* **2015**, *7*, 1208–1214. [[CrossRef](#)]



© 2016 by the authors; licensee MDPI, Basel, Switzerland. This article is an open access article distributed under the terms and conditions of the Creative Commons Attribution (CC-BY) license (<http://creativecommons.org/licenses/by/4.0/>).